

Article

Numerical Study on Hydrodynamic Performance of a Pitching Hydrofoil with Chordwise and Spanwise Deformation

Hengliang Qu ^{1,2}, Xueyan Li ^{1,2,*} and Xiaochen Dong ³

¹ School of Hydraulic Engineering, Ludong University, Yantai 264025, China; quhenngliang@ldu.edu.cn

² Institute of Coast & Sea-Crossing Engineering, Ludong University, Yantai 264025, China

³ Shandong Provincial Key Laboratory of Ocean Engineering, Ocean University of China, Qingdao 266100, China; dongxiaochen@ouc.edu.cn

* Correspondence: yanzi03@126.com

Abstract: The hydrofoil plays a crucial role in tidal current energy (TCE) devices, such as horizontal-axis turbines (HATs), vertical-axis turbines (VATs), and oscillating hydrofoils. This study delves into the numerical investigation of passive chordwise and spanwise deformations and the hydrodynamic performance of a deformable hydrofoil. Three-dimensional (3D) coupled fluid–structure interaction (FSI) simulations were conducted using the ANSYS Workbench platform, integrating computational fluid dynamics (CFD) and finite element analysis (FEA). The simulation involved a deformable hydrofoil undergoing pitching motion with varying elastic moduli. The study scrutinizes the impact of elastic modulus on hydrofoil deformation, pressure distribution, flow structure, and hydrodynamic performance. Coefficients of lift, drag, torque, as well as their hysteresis areas and intensities, were defined to assess the hydrodynamic performance. The analysis of the correlation between pressure distribution and deformation elucidates the FSI mechanism. Additionally, the study investigated the 3D effects based on the flow structure around the hydrofoil. Discrepancies in pressure distribution along the spanwise direction result from these 3D effects. Consequently, different chordwise deformations of cross-sections along the spanwise direction were observed, contributing to spanwise deformation. The pressure difference between upper and lower surfaces diminished with increasing deformation. Peak values and fluctuations of lift, drag, and torque decreased. This study provides insights for selecting an appropriate elastic modulus for hydrofoils used in TCE devices.



Citation: Qu, H.; Li, X.; Dong, X. Numerical Study on Hydrodynamic Performance of a Pitching Hydrofoil with Chordwise and Spanwise Deformation. *J. Mar. Sci. Eng.* **2024**, *12*, 830. <https://doi.org/10.3390/jmse12050830>

Academic Editor: Dejan Brkić

Received: 26 April 2024

Revised: 13 May 2024

Accepted: 14 May 2024

Published: 16 May 2024



Copyright: © 2024 by the authors. Licensee MDPI, Basel, Switzerland. This article is an open access article distributed under the terms and conditions of the Creative Commons Attribution (CC BY) license (<https://creativecommons.org/licenses/by/4.0/>).

Keywords: numerical study; hydrodynamic performance; pitching hydrofoil; chordwise deformation; spanwise deformation

1. Introduction

A pitching hydrofoil can function directly as a tidal current energy (TCE) device [1,2]. The rotating blades of the horizontal-axis turbine (HAT) and vertical-axis turbine (VAT) devices can also be considered as pitching foils [3,4]. Pitching hydrofoils have garnered increasing attention, and extensive research has been conducted on their hydrodynamic performance [5–7]. The TCE device with an oscillating hydrofoil undergoes multi-degree-of-freedom motion in response to hydrodynamic forces or torques. HAT and VAT TCE devices exhibit rotational motion driven by the lift exerted on the blades [8]. The hydrodynamic performance of a hydrofoil is directly influenced by its flow structure in the vicinity of the foil [9,10]. The flow structure is determined by fluid–structure interaction (FSI), which is affected by motion parameters (pitching amplitude, tip speed ratio, and reduced frequency) [11], structural parameters (cross-section, pivot location, and aspect ratio) [12], and environmental dynamic parameters (Reynolds number and turbulence intensity) [13]. Hydrofoil deformation can optimize the surrounding flow structure and hydrodynamic characteristics, leading to improved energy harvesting in devices with deformable hydrofoils [14–16]. Consequently, deformable hydrofoils have recently gained considerable attention in the study of the hydrodynamic performance of deformable pitching hydrofoils.

Experimental studies have been conducted to investigate the effects of pitching rate on the hydrodynamic performance and flow regime transition of the pitching hydrofoil. The results indicate that a higher pitching rate promotes separation, delays dynamic stall, and suppresses hydrodynamic force fluctuations [6]. Additionally, numerical investigations have been carried out to analyze the effects of the pitching pivot location on the dynamic stall characteristics of a passive pitching hydrofoil. The results indicate that backward movement of the pitching pivot leads to a noticeable hysteresis effect [17]. Simultaneously, the evolution of the leading-edge vortex (LEV) is delayed [18]. Non-sinusoidal pitching motion of the foil was found to promote transitions in the drag-thrust [19,20]. The pitching method and frequency of a hydrofoil were found to have a significant influence on flow separation and hydrodynamic performance [21]. The effects of a vane-type vortex generator on the dynamic stall of a pitching foil were numerically studied. Reports indicate that a vortex generator can suppress unsteady flow separation and dynamic stall, while simultaneously improving lift [22]. The hydrodynamic stall, hysteresis effect, and hydrodynamic force fluctuations of hydrofoils are currently under investigation by several researchers.

Deformable hydrofoils based on bionics have been proposed and studied across various fields to enhance hydrodynamic performance. Hydrofoil deformation can be categorized into two types: activated and passive deformations. The activated type implies artificially controlled deformation, while the passive type involves deformation governed by water flow and hydrofoil stiffness [23]. A chordwise deformable foil for a VAT was experimentally studied under quasi-steady conditions, with deformation controlled by a built-in mechanical structure. Reports indicate that lift coefficient and lift-to-drag ratio increase with greater flexure, delaying the stall attack angle [24]. Activated trailing edge deformation with appropriate parameters can reduce lift fluctuation of the pitching foil for HAT [25]. Numerical studies on the energy-harvesting performance of an oscillating hydrofoil with activated chordwise deformation showed improved lift and energy-harvesting capabilities due to increased pressure difference between upper and lower surfaces [26–28]. Passive chordwise deformation increased the effective angle of attack, modulating the magnitude and phase of dynamic force for enhanced energy harvesting performance [29]. Passive chordwise deformation keeps the LEV closer to the foil surface, inducing low pressure [30]. Compared to activated deformation, passive deformation without a complex mechanism structure is more feasible for practical applications. Therefore, this study aims to investigate the hydrodynamic performance of a passively deformable pitching hydrofoil.

Deformable hydrofoils have been primarily studied using a two-dimensional (2D) numerical model, without considering the three-dimensional (3D) effect. However, the 3D effect, which is influenced by the finite span length of the hydrofoil, significantly impacts hydrodynamic performance [31]. Vortex structures around a 3D hydrofoil are different from those around a 2D hydrofoil, resulting in a pressure distribution difference. Consequently, the power coefficient of the 3D hydrofoil drops by 20 to 30% compared to the 2D hydrofoil due to tip loss. Numerical studies on the effects of aspect ratio on vortex structure around a 3D hydrofoil reveal that tip vortices merge into a 3D vortex ring at a low aspect ratio. As the aspect ratio increases to four, tip vortices stretch and form elongated loops [32]. The 3D effect becomes less pronounced when the aspect ratio exceeds four [33]. Experimental studies on the effects of aspect ratio on the LEV, with vortex structures measured using particle image velocimetry (PIV), show LEV growth suppression by a 3D tip flow at a low aspect ratio [34]. The 3D effect leads to differences in flow structure, pressure distribution, and hydrodynamic force along the spanwise direction of the hydrofoil. Consequently, the chordwise deformations in different spanwise sections also vary. The spanwise deformations of the hydrofoil have an influence on hydrodynamic performance. A spanwise deformable hydrofoil can generate higher lift than a rigid hydrofoil at small angles of attack [35,36].

Previous research has separately examined the effects of chordwise and spanwise deformations. However, these deformations usually occur simultaneously. Consequently, we examined the impact of coupled chordwise and spanwise deformations on the hydrody-

dynamic performance of the hydrofoil. A hydrofoil with the passive deformation and pitching motion deviates from a static state and aligns more closely with the motion characteristics of blades in HAT, VAT, or oscillating hydrofoils. Previous research solely focused on spanwise deformation without considering the 3D flow effect. Therefore, our study aims to address the interaction between the 3D flow effect and 3D deformation.

A 3D numerical model for a passively deformable hydrofoil was established using ANSYS Workbench 16.0. The model's validity was confirmed through experimental and numerical results. Limited by the simulation technology, previous studies have generally utilized the one-way FSI numerical model, which ignores the effects of deformation on the flow field. In addition, the numerical simulations in previous studies have widely utilized steady-state calculations based on the Multiple Reference Frame (MRF) model. The numerical model in this paper uses the transient state calculation based on sliding mesh technology. The hydrofoil implements the pitching motion as real. The numerical simulation employs a two-way FSI solved by coupling CFD and FEA modules [37]. This two-way FSI numerical simulation method, utilizing mature, stable, and widely applicable commercial software, involves the transfer of pressure calculated by the CFD module to the FEA module for solving structural deformation. The deformation is then transferred back to the CFD module, renewing the structure's boundary and recalculating the flow field. This method simulates a real physical process, reproducing the operating status of a deformable hydrofoil. We explore the effects of elastic modulus on the hydrofoil's deformation, pressure distribution, flow structure, and hydrodynamic performance. Additionally, the FSI mechanism of the deformable hydrofoil is discussed. Given the hydrofoil's significance in TCE devices, the hydrodynamic performance of the pitching hydrofoil can indicate energy-harvesting performance to some extent [38,39]. This study contributes technical support and theoretical insights for the blade design of TCE devices.

Section 2 provides a comprehensive introduction to the hydrofoil's structure, parameters, kinematic equations, and hydrodynamic performance indicators. The numerical model setup and validation are detailed in Section 3. In Section 4, the deformation, hydrodynamic performance of the hydrofoil, flow structure, and pressure distribution are presented and analyzed. Conclusions and future work are presented in Section 5.

2. Passively Deformable Hydrofoil under Activated Pitching Mode

A passively deformable hydrofoil in the activated pitching mode is shown in Figure 1. The incident flow velocity was set to $U = 0.4$ m/s. The cross-sectional profile of the undeformed hydrofoil was NACA0010, and the chord length C was 0.12 m. The pitching frequency and amplitude were set to 0.2 Hz and 60° , respectively. The dimensionless reduced frequency, defined as $f^* = fC/U$, was 0.06. The span length of the hydrofoil S was set to 0.4 m. The pitching pivot O was located on the center-chord line at a distance of $C/3$ from the leading edge. Assuming that a stainless-steel shaft penetrates and supports the hydrofoil through pivot O , the hydrofoil does not bend in the spanwise direction. The leading segment (from the leading edge to pivot O) was considered rigid. Deformation occurred in the trailing segment (from Pivot O to the trailing edge). The chordwise deformations of various cross-sections in the spanwise direction were different owing to the 3D effect. The chordwise deformation difference was defined as the spanwise deformation. δ is the deformation of the trailing edge. The cross-section $Z = 0$ was set at the midpoint in the spanwise direction. The cross-section $Z = S/2$ was set at the tip of the hydrofoil. In this study, the hydrofoil is designed as a solid structure manufactured using 3D printing technology. In addition, the polyethylene material is nontoxic, waterproof, and anti-corrosion from acid and alkaline, which is suitable for operation in actual operating environments. Therefore, the properties of the hydrofoil were set according to the polyethylene. The elasticity modulus E of the deformable hydrofoil was set to 2, 4, or 6 MPa. The density and the Poisson ratio were set as 0.98×10^3 kg/m³ and 0.48.

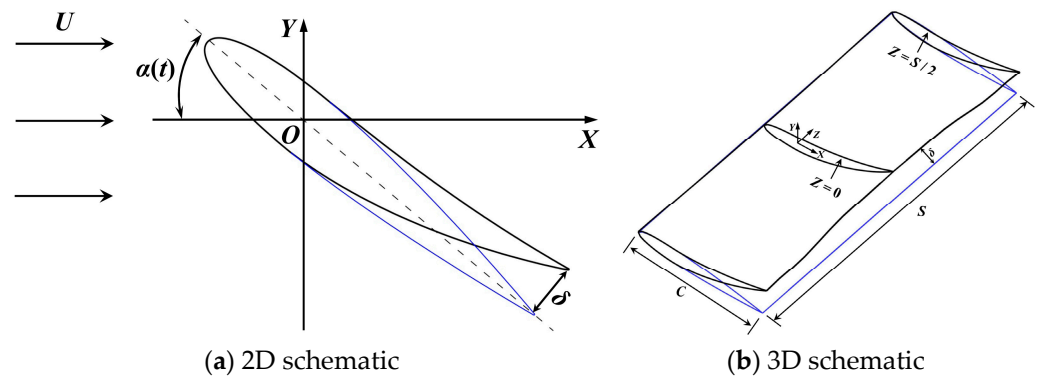


Figure 1. Passively deformable hydrofoil under activated pitching mode.

The governing equation for the single-activated pitching motion over pivot O is as follows:

$$\alpha(t) = \alpha_0 \cos(2\pi ft) \tag{1}$$

where $\alpha(t)$ is the instantaneous prescribed pitching angle at the time point t , α_0 is the pitching amplitude, and f is the pitching frequency.

The instantaneous lift, drag, and hydrodynamic torque coefficients are defined as follows:

$$C_L = \frac{L}{0.5\rho U^2 SC} \tag{2}$$

$$C_D = \frac{D}{0.5\rho U^2 SC} \tag{3}$$

$$C_M = \frac{M}{0.5\rho U^2 SC^2} \tag{4}$$

where L , D , and M are the lift, drag, and hydrodynamic torque, respectively, and ρ is the water density.

To quantitatively evaluate the hysteresis effects of the deformable pitching hydrofoil, the hysteresis areas of C_L , C_D , and C_M were defined, as follows [5,40]:

$$A_{CL} = \int_{-T}^T |C_{L-U}(t) - C_{L-D}(t)| dt \tag{5}$$

$$A_{CD} = \int_{-T}^T |C_{D-U}(t) - C_{D-D}(t)| dt \tag{6}$$

$$A_{CM} = \int_{-T}^T |C_{M-U}(t) - C_{M-D}(t)| dt \tag{7}$$

where $C_{L-U}(t)$ and $C_{L-D}(t)$ are the lift coefficients in the upstroke and downstroke stages, respectively; $C_{D-U}(t)$ and $C_{D-D}(t)$ are the drag coefficients in the upstroke and downstroke stages, respectively; $C_{M-U}(t)$ and $C_{M-D}(t)$ are the torque coefficients in the upstroke and downstroke stages, respectively; and T is the pitching period.

The hysteresis intensities of C_L , C_D , and C_M are defined as follows [40].

$$K_L = \frac{C_{L-\max} - C_{L-\min}}{T_{\max} - T_{\min}} \tag{8}$$

$$K_D = \frac{C_{D-\max} - C_{D-\min}}{T_{\max} - T_{\min}} \tag{9}$$

$$K_M = \frac{C_{M-\max} - C_{M-\min}}{T_{\max} - T_{\min}} \tag{10}$$

where C_{L-max} , C_{D-max} and C_{M-max} denote the maximum lift, drag, and torque coefficients, respectively; C_{L-min} , C_{D-min} and C_{M-min} are the minimum lift, drag, and torque coefficients, respectively; and T_{max} and T_{min} denote the time points at which the maximum and minimum values are obtained, respectively.

The pressure coefficient C_p is defined as follows:

$$C_p = \frac{p}{0.5\rho U^2} \tag{11}$$

where p is the pressure around the hydrofoil's surface.

3. Numerical Model

3.1. Numerical Model Set-Up

A transient numerical model of the passively deformable hydrofoil was established based on the computational platform ANSYS Workbench 16.0, which incorporated CFD and FEA solvers. The flow field was calculated using the CFD solver Fluent 16.0. The structural field was calculated using the FEA solver Transient Structural 16.0. Both solvers were connected through a System Coupling module to implement a two-way FSI simulation. A flowchart of the two-way FSI numerical simulation is presented in Figure 2. After initialization, the flow field and pressure distribution were calculated using a CFD solver. The pressure data were then transferred to the FEA solver through the fluid–structure interface. Subsequently, the deformation and pitching motions of the hydrofoil were solved. The structural boundary was updated. The updated boundary position was simultaneously transferred to the CFD solver. This process was repeated in subsequent time steps, forming a new cycle of calculations.

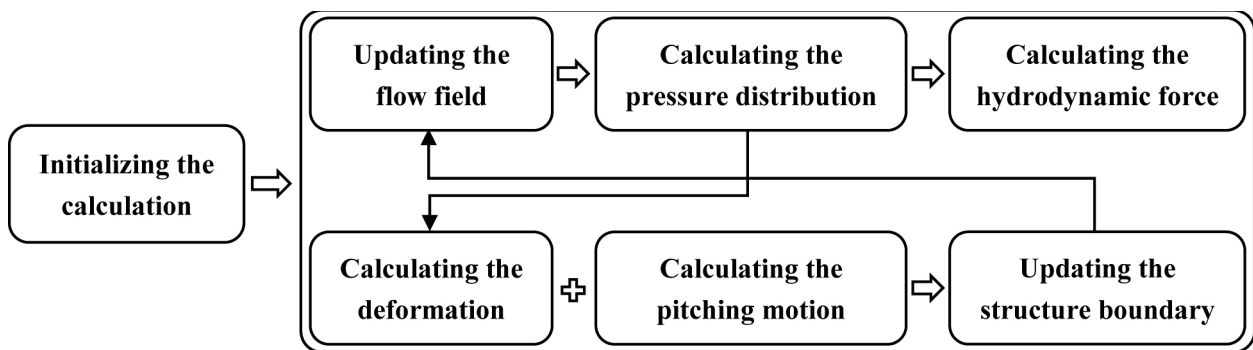


Figure 2. Flow chart of the two-way FSI numerical simulation.

The basic governing equation of the transient dynamics of the passively deformed hydrofoil can be written as follows [37]:

$$[M]\{u''\} + [C]\{u'\} + [K]\{u\} = \{F(t)\} \tag{12}$$

where $[M]$, $[C]$, and $[K]$ represent the mass, damping, and stiffness matrices, respectively; $\{u''\}$, $\{u'\}$, and $\{u\}$ represent the vectors of the acceleration, velocity, and displacement on the node, respectively; and $\{F(t)\}$ is the resultant force vector.

A schematic of the numerical model is shown in Figure 3. The computational domain consists of fluid and structural domains. The length, width, and height of the fluid domain are $12 C$, $7 C$, and $6 C$, respectively. The left and right sides of the fluid domain were set as the inlet velocity and outlet pressure boundaries, respectively. Pivot O was located at a distance of $5 C$ and $7 C$ from the velocity inlet and pressure outlet boundaries, respectively. The other sides of the fluid domain were set as symmetrical boundaries. The tips of the hydrofoils were C away from the top and bottom sides. The fluid domain was divided into outer and inner pitching zones. The two zones were connected by interfaces that conduct

data exchange. Sliding mesh technology was employed. The pitching zone rotated with the pitching hydrofoil along the interface.

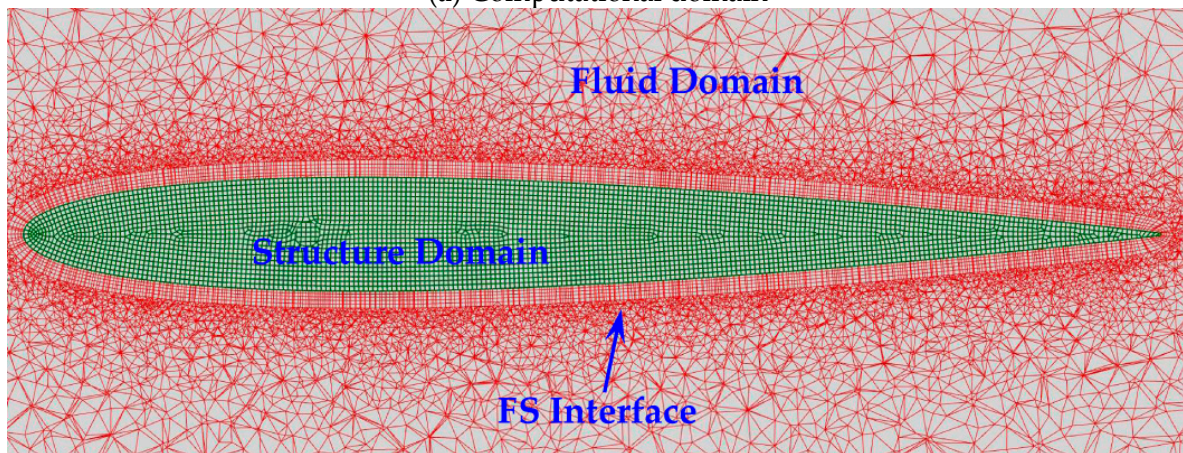
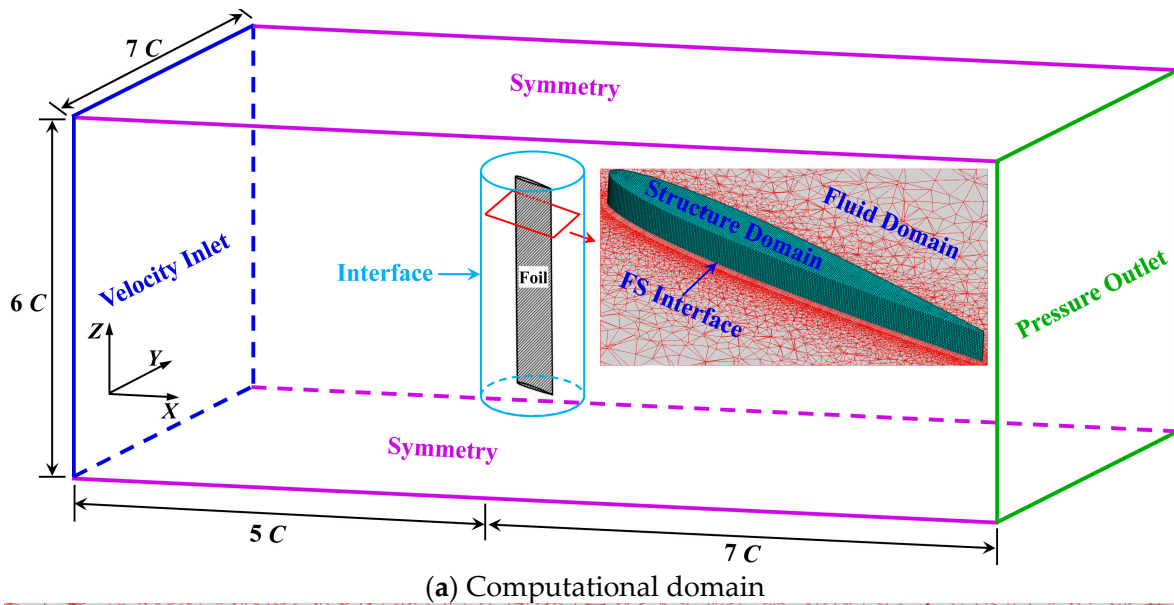


Figure 3. Computational domain and meshes of numerical model.

As shown in Figure 3b, unstructured meshes were used in the fluid domain. Structured boundary layer meshes were applied to the wall boundary of the fluid domain. The grid size of the first layer meshes was set as 0.5 mm. The number of the boundary layer meshes was 5, with a growth rate of 1.05. The value of Y^+ for the meshes of the first layer was maintained below 5.0 under various conditions. Both the structured boundary layer and unstructured meshes were synchronized with the pitching zone, preventing significant mesh deformation resulting from the pitching motion. The mesh deformation caused by the hydrofoil deformation was relatively limited. The CFD solver, Fluent 16.0, provides a smoothed dynamic mesh technology that controls the deformation of the boundary layer meshes. The element sizes of the outer boundaries and foil wall boundary of the fluid domain were set to 30.0 mm and 0.5 mm, respectively. The total number of meshes in the fluid domain was 14.0 million.

Unstructured meshes were employed in the structure domain with a mesh size of 0.5 mm, and the total number of meshes in the structure domain was 3.2 million. In the FEA solver, Transient Structural 16.0, the virtual pivot O was set on the hydrofoil. The rotational velocity joint was established on the virtual pivot O . The governing equation (1) was compiled on the rotational velocity joint to control the activated pitching motion.

The FEA solver calculated the deformation and activated pitching motion. The position information of each cell was obtained.

The fluid–structure interfaces were formed by the foil wall boundary of the fluid domain and the foil boundary of the structure domain. To transfer information on pressure and position from the wall boundary, interpolation mapping was used on the fluid–structure interfaces. The interpolation process consisted of 10 iteration steps and used a convergence criterion of 10^{-6} .

The standard k - ω model has good performance in predicting boundary layer flow, separation, and transition in the presence of reverse pressure gradient. Therefore, the standard k - ω model was selected to deal with turbulent problems. The pressure–velocity coupling employed the SIMPLE (semi-implicit method for the pressure-linked equation) scheme. The derivatives were calculated based on the Green–Gaussian nodes. A second-order upwind scheme was applied for the spatial discretization of the momentum, turbulent kinetic energy, and specific dissipation rate. The temporal term was discretized using a second-order implicit scheme. The convergence criterion was set at 10^{-6} . In this model, the CFD, FEA, and system coupling modules utilized the same time-step size of $0.005 T$ and 50 iterations per time step. The detailed information of the numerical model is listed in Table 1.

Table 1. Information of the numerical model.

Description	Set-Up
Time-step size	$0.005 T$
Iteration per time step	50
Mesh type of fluid domain	Tetrahedral mesh
Grid size on outer boundaries of fluid domain	30.0 mm
Grid size on foil wall boundary of fluid domain	0.5 mm
Growth rate of boundary layer mesh	1.05
Mesh type of structure domain	Hexahedral mesh
Grid size of structure domain	0.5 mm
Turbulence model	Standard k - ω model
Convergence criterion	10^{-6}

3.2. Numerical Model Validation

The capability of solving the structural deformation, flow field, and the data transfer between the FEA and CFD solvers were validated through multiple cases. The oscillations of a vertical deformable plate normal to a free stream were simulated and compared to validate the accuracy of the FEA solver and the capability of data transfer in the two-way FSI numerical model. The length, thickness, and width of the deformable plates were 1.0 m, 0.06 m, and 0.4 m, respectively. The elastic modulus and density of the deformable plate were 2.5 MPa and 2550 kg/m^3 , respectively. An initial uniform load of 30 N/m was applied to the deformable plate and released at time $t = 0.5 \text{ s}$. The damped oscillations of the deformable plate were also recorded. Similar investigations were conducted using 3D simulations in references [41,42]. The displacements at the free end of the deformable plate are compared in Figure 4. The displacement of the free end of the deformable plate d and the oscillation frequency of the proposed model agreed well with the results of previous studies. The average relative errors of the displacement amplitude between the present numerical model and the numerical models in Refs. [41,42] were 6.8% and 11.2%, respectively.

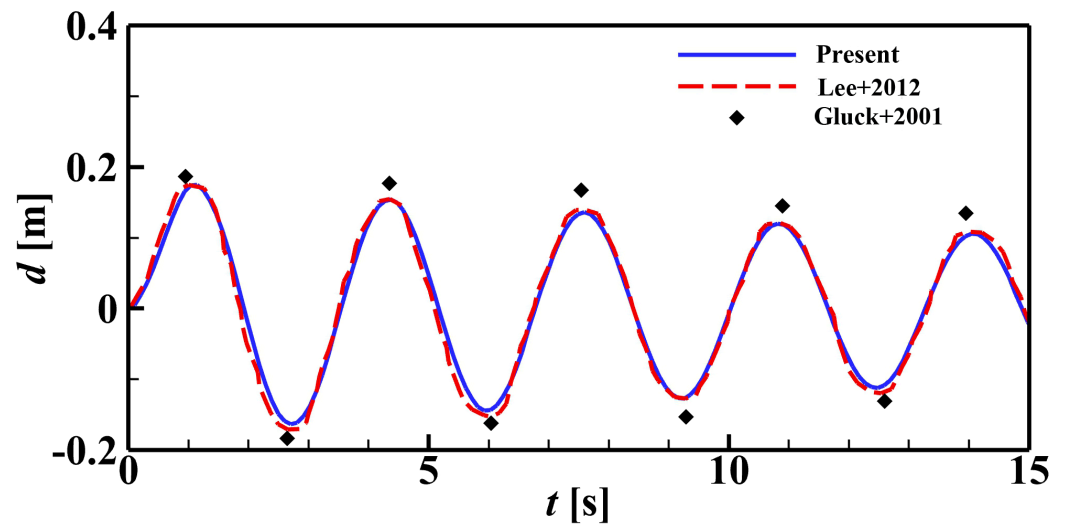


Figure 4. The displacement of the free end of the deformable plate [41,42].

As shown in Figure 5, an experiment of the flexible plate undergoing single activated-pitching was conducted, and the numerical and experimental results of the tip deformation were compared to validate the numerical model. The chord length, span length, and thickness of the plate were 0.12 m, 0.4 m, and 0.008 m, respectively. The incident flow velocity was set to $U = 0.4$ m/s. The pitching frequency and amplitude were set to 0.2 Hz and 60° , respectively. The instantaneous tip deformation of the plate was measured based on a digital imaging algorithm. Detailed information regarding the experiment facility and technology was given in our previous study [43]. The average relative difference between the numerical and experimental tip deformations was 7.3%. The above validation demonstrates the capability and accuracy of solving structural deformation and transferring data.

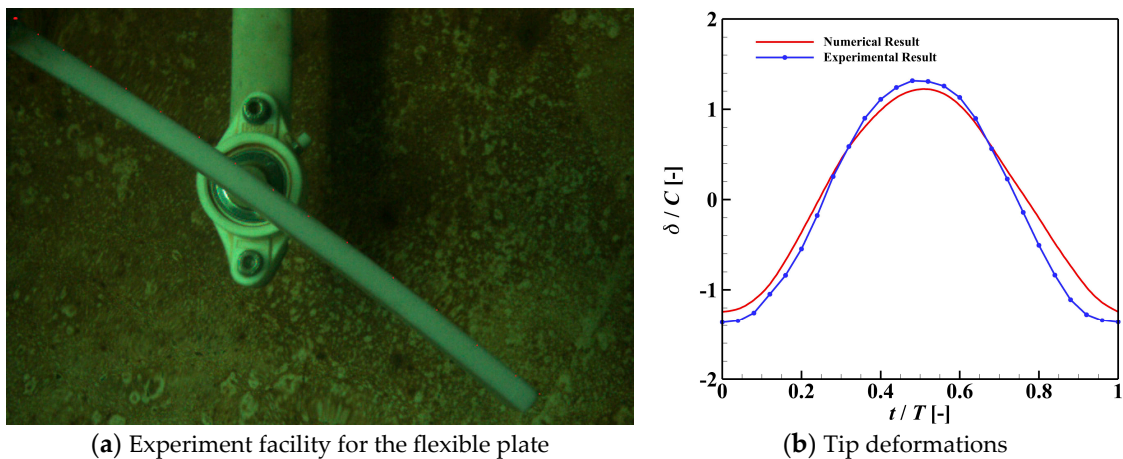


Figure 5. Comparison of numerical and experimental deformations.

The Spalart-Allmaras (S-A), Shear-stress transport (SST), and $k-\omega$ turbulence models are widely used in the numerical simulations of hydrofoils [12]. The numerical results for the abovementioned turbulence models were compared to select a reliable turbulence model. Then, the numerical results were compared with the experimental results to validate the capability and accuracy of solving the flow field. The numerical simulation conditions and the experimental results come from previous studies [3,44]. The NACA0012 foil with chord length of 0.1 m and span length of 0.38 m was experimentally tested under the Reynolds number of 2.3×10^4 . The pitching amplitude and reduced frequency of the foil were 6° and 0.1, respectively. The experimental conditions were similar to those used in

the numerical study. A comparison between C_L and C_D is shown in Figure 6. As shown in Figure 6a, the numerical results of C_L and C_D for various turbulence models were similar. A limited difference occurred at a higher pitching angle. Considering the computational cost and accuracy, the Standard $k-\omega$ turbulence model was selected in subsequent simulations.

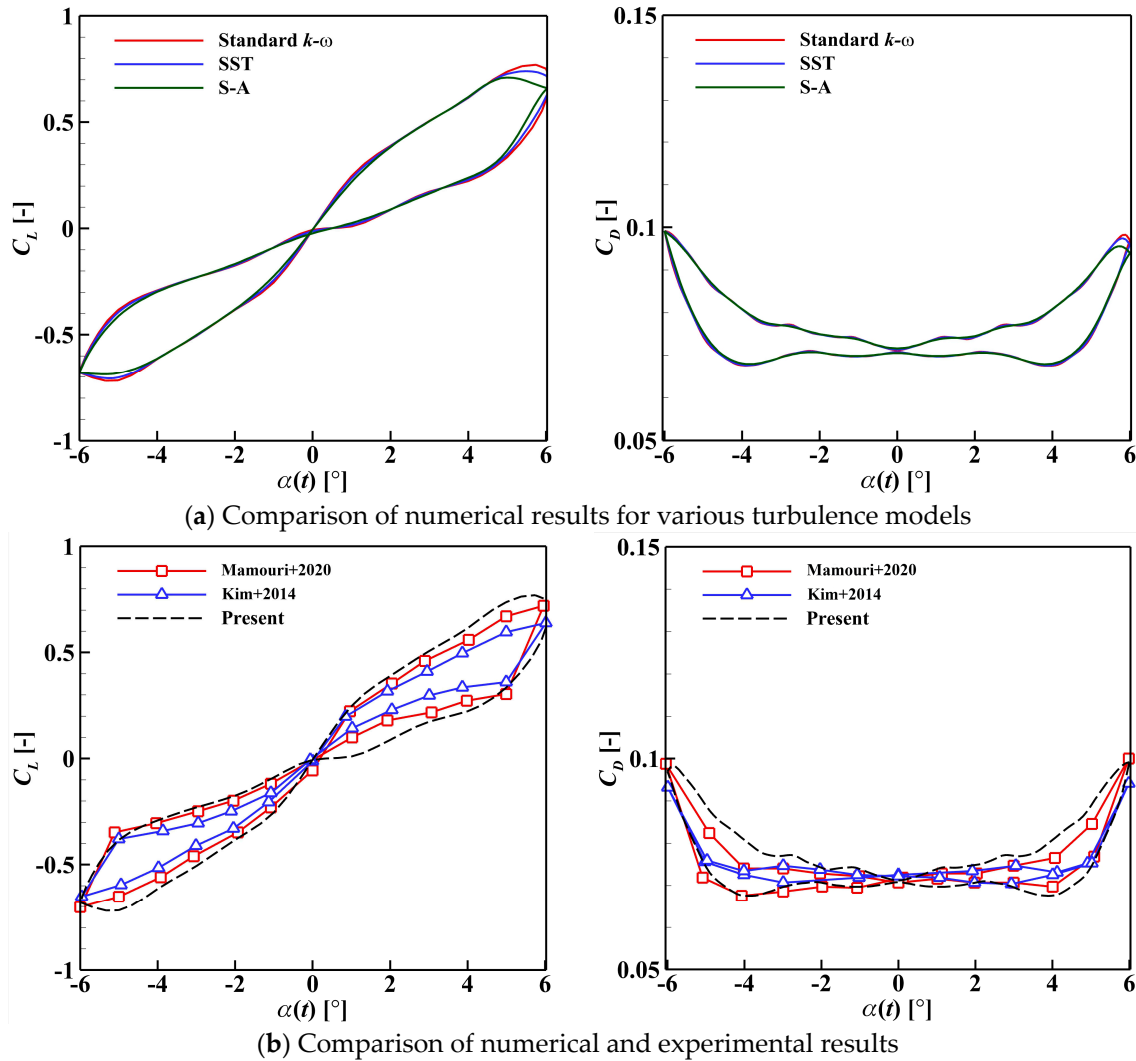


Figure 6. The comparison of C_L and C_D [3,44].

As shown in Figure 6b, the hysteresis curve patterns of the numerical C_L and C_D were similar to those of the experimental C_L and C_D . The average error in C_L between the present numerical model and [3] was 8.3%. The average error of C_D was 9.7%. From the above validation, it can be concluded that the proposed numerical model demonstrates its capability with regard to the flow field solution. The 3D FSI numerical model can be applied in future investigations.

4. Results and Discussion

The deformation, pressure coefficient, flow structure, and hydrodynamic coefficients of the hydrofoil are presented and analyzed to reveal the FSI mechanism in depth. The effects of chordwise and spanwise deformations on the hydrodynamic performance of an activated pitching hydrofoil were investigated under various elastic moduli.

4.1. Flow Structure and Pressure Distribution around the Rigid Hydrofoil

A rigid hydrofoil served as the basis for comparison. The flow structures and pressure distributions around the hydrofoil in the fore-half cycle were symmetrical to those in the rear-half cycle. The 3D streamlines around the rigid hydrofoil at $t = 3T/4$ and T are shown in Figure 7. The color of the streamlines represents the magnitude of velocity. At $t = 3T/4$, the instantaneous pitching angle $\alpha(3T/4)$ is 0° , namely, the chord line of the hydrofoil is parallel to the incident flow. The instantaneous pitching angular velocity reaches its peak value. At $t = T$, the instantaneous pitching angle reaches its peak value, and the pitching angular velocity becomes 0.

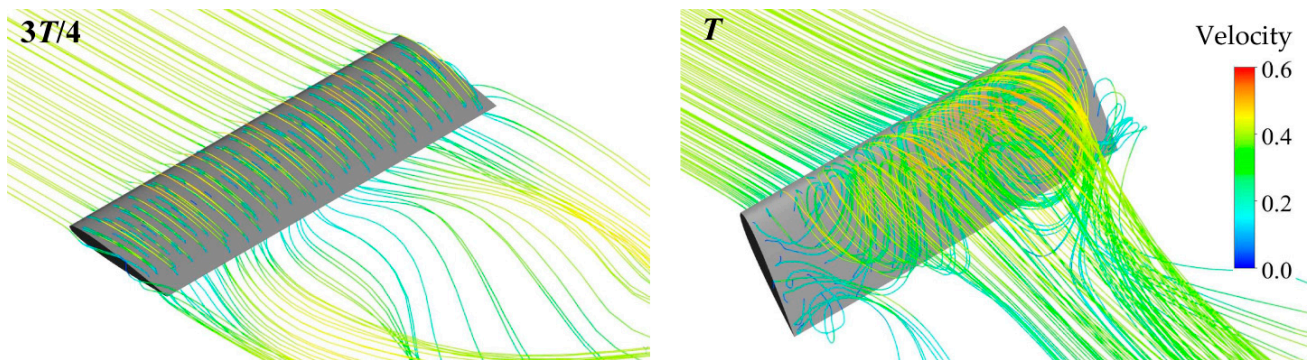


Figure 7. Three-dimensional streamlines around rigid hydrofoil.

At $t = 3T/4$, the streamlines over the upper surface exhibited a uniform distribution along the spanwise direction. Conversely, the streamlines over the lower surface exhibited a distinctly nonuniform distribution. The streamlines curled from the lower to the upper surfaces near the hydrofoil tips. Additionally, in the midspan region, the streamlines sharply ascended and dispersed in the wake area. Moreover, the streamlines in other areas gradually curved upward.

At $t = T$, the streamlines over the lower surface exhibited a relatively uniform distribution in the spanwise direction. The streamlines over the upper surface formed distinct vortex structures. The streamlines near the hydrofoil tips established a circulatory motion and flowed downstream, indicating the formation of a tip vortex. Spiral streamlines were generated from the leading edge and converged to the midspan region before flowing downstream. A non-uniform distribution of streamlines was generated on the pressure surface of the hydrofoil due to the 3D effect. The 3D effect becomes more pronounced when the hydrofoil has a large pitch angle. The distributions of the vortex and pressure along the spanwise direction were discussed to study the 3D effect.

The flow structures in the spanwise direction were symmetrical about the midspan cross-section. The flow structures of the half-span hydrofoil were analyzed. The 2D streamlines and vortices around the rigid hydrofoil at various Z positions are shown in Figure 8. The positions $Z = 0$ and $Z = S/2$ represent the midspan and hydrofoil tip cross-sections, respectively. The streamlines and vortices exhibited significant differences at various Z positions. The color label represents the vorticity intensity.

As shown in Figure 8a, a small clockwise LEV was generated and attached to the upper surface at $Z = 0$. A counterclockwise vortex was generated and developed at the trailing edge. Vortex shedding occurred downstream of the trailing edge. The streamlines that flow through the counterclockwise vortex and vortex shedding were significantly curved. At $Z = S/8$, both the upper and lower surfaces were covered by the attached vortex. The distance from the shedding vortex to the trailing edge increased slightly. The flow structure over the hydrofoil surface at $Z = S/4$ was similar to that at $Z = S/8$. The shedding vortex developed downstream of the wake area. At $Z = S/2$, the scale and intensity of the vortex on the lower surface decreased. The streamlines became smoother.

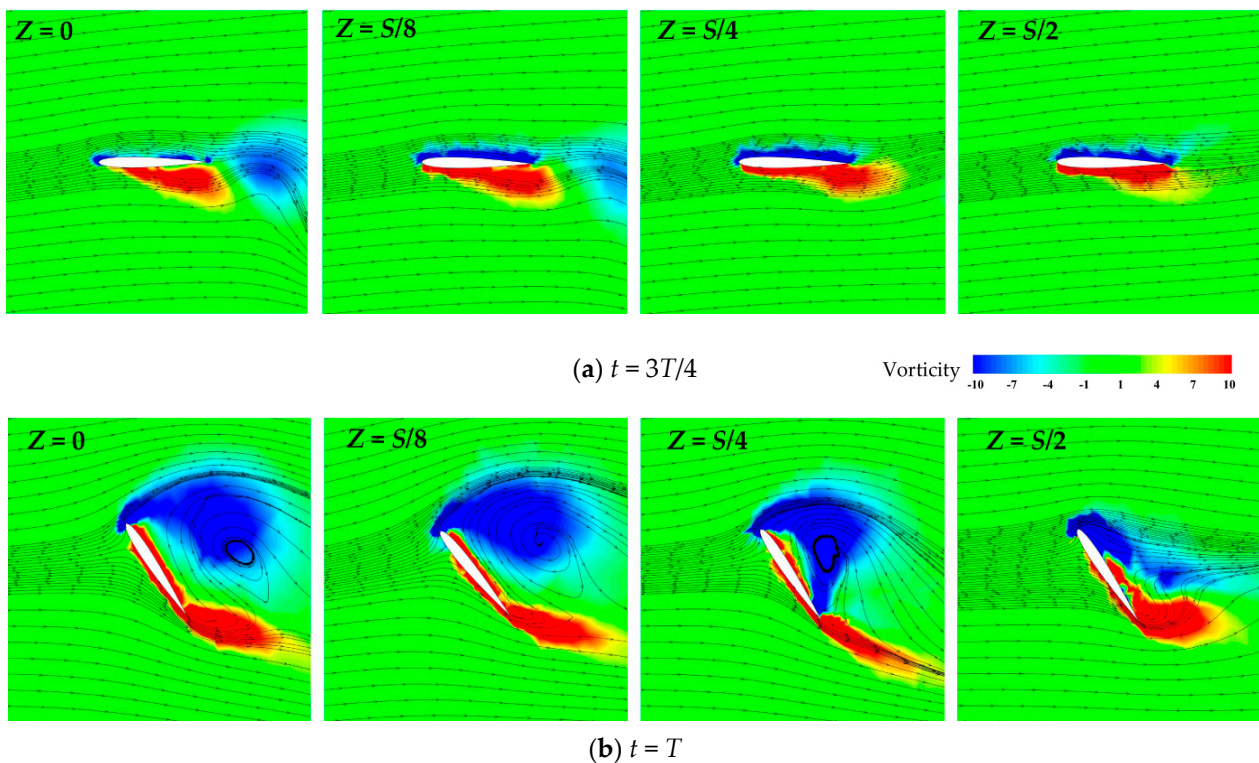


Figure 8. Flow structures around the rigid hydrofoil at various Z positions.

As shown in Figure 8b, a significant clockwise LEV was formed above the hydrofoil at $Z = 0$. A counter-clockwise TEV was formed behind the hydrofoil. The surface of the hydrofoil was covered with a slender attached vortex. The streamlines were sharply curved under the effects of the vortex, indicating the occurrence of reverse flow. Some streamlines from the lower surface flipped over to the upper surface, bypassing the trailing edge. These streamlines then reached the leading edge along the upper surface. Subsequently, the streamlines flowed through the LEV and changed direction. The flow structure over the hydrofoil surface at $Z = S/8$ was similar to that at $Z = 0$. At $Z = S/4$, a clockwise LEV developed over the upper surface and attached to the trailing edge. At $Z = S/2$, the size and intensity of the LEV decreased significantly. The TEV developed from the upper surface to the midchord position. Changes in the vortex distribution were caused by the interaction of the tip vortex. The streamline distributions at various Z positions indicate that the reverse flow was attenuated with diminished LEVs.

Based on the above analysis, it is evident that there is a component of the flow in the spanwise direction, meaning that the flow over the hydrofoil is three-dimensional. The difference in the flow structures at various Z positions resulted in a difference in the pressure distribution. The pressure distributions around the rigid hydrofoil at various Z positions are shown in Figure 9. The color label represents the nondimensional deformation based on the chord length C . The deformation of the rigid hydrofoil was 0.

At $t = 3T/4$, the pressure coefficient on the upper surface was mainly negative. In contrast, the pressure coefficient on the lower surface was mainly positive. The pressure difference between the lower and upper surfaces caused the flow near the tips to curl from the lower surface to the upper surface, bypassing the tips. This phenomenon influenced the pressure distribution in the spanwise direction. The pressure difference between the upper and lower surfaces at $Z/S = 0.5$ was 0.52, which was obviously less than the pressure differences at the other Z positions. The maximum pressure coefficient difference was 0.98, which was obtained at $Z/S = 0.25$.

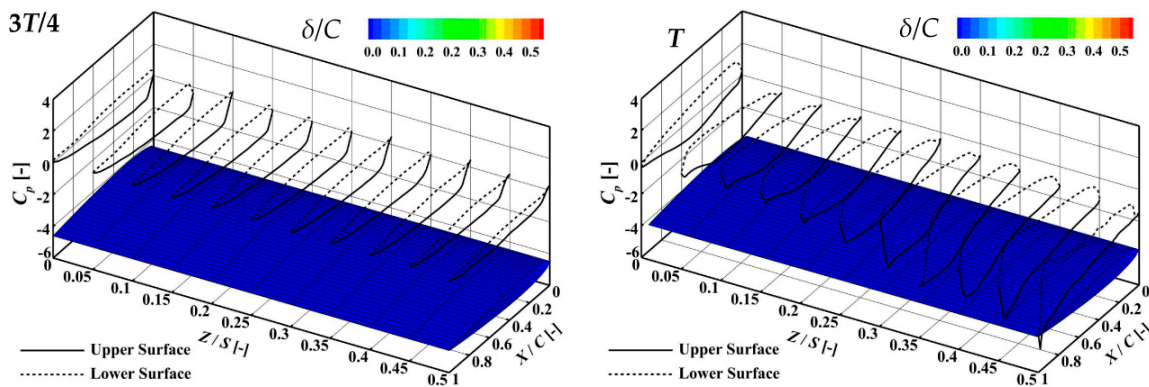


Figure 9. Pressure distribution around the rigid hydrofoil.

At $t = T$, the pressure coefficient on the upper surface was mainly negative. The pressure coefficient on the lower surface at most Z positions was mainly positive, except for the pressure coefficient at $Z/S = 0.5$. The pressure coefficient difference between the upper and lower surfaces at $Z/S = 0.5$ was 1.51. The maximum pressure coefficient difference of 2.13 was obtained at $Z/S = 0.25$. The minimum pressure coefficient difference of 1.40 was obtained at $Z/S = 0$. The differences in the pressure distribution at various Z positions were closely correlated with the non-uniform distributed flow structures shown in Figure 7. The high pressure at $Z/S = 0.25$ resulted in the streamlines concentrating in the midspan region and bending over the tips. Furthermore, the differences in the pressure distribution leads to deformation differences in the chordwise and spanwise directions, which are analyzed in the next subsection.

4.2. Deformation, Flow Structure, and Pressure Distribution of the Deformable Hydrofoil

The flow structure, pressure distribution, and deformation of the deformable hydrofoil at various elastic moduli in the rear-half cycle are presented. The relationship between the abovementioned three parameters is studied to reveal the FSI mechanism of the deformable hydrofoil.

The 3D streamlines around the deformable hydrofoil at various elastic moduli are shown in Figure 10. At $t = 3T/4$, the streamlines over the upper surface were limited by the elastic modulus. Certain differences in the streamlines over the lower surface were observed under various elastic moduli. For $E = 2$ MPa, as shown in Figure 10a, the streamlines near the midspan deflected downward from the trailing edge immediately and then deflected upward in the wake. As shown in Figures 7 and 10b,c, the magnitude of downward bending near the midspan decreases as the elastic modulus increases. The curling from the lower surface to the upper surface of the streamlines near the hydrofoil tips gradually disappeared with decreasing elastic modulus. A certain upward deformation for $E = 2$ MPa was observed between the midspan and tip of the hydrofoil. This deformation leads to an invagination on the lower surface, which suppresses the curling of the streamlines.

At $t = T$, the streamline pattern varies with the elastic modulus. At $E = 2$ MPa, as shown in Figure 10a, evident deformation and curling of the streamlines occurred at the hydrofoil tips. As shown in Figures 7 and 10b,c, the deformation and curling of the streamlines gradually decreased with increasing elastic modulus. It can be observed that the deformation increases as the elastic modulus decreases. This implies that the deformation at the hydrofoil tips contributed to the curling of the streamlines. Spanwise deformation causes the upward bending of the tips, which promotes the curling of the streamlines at the hydrofoil tips and the formation of tip vortices.

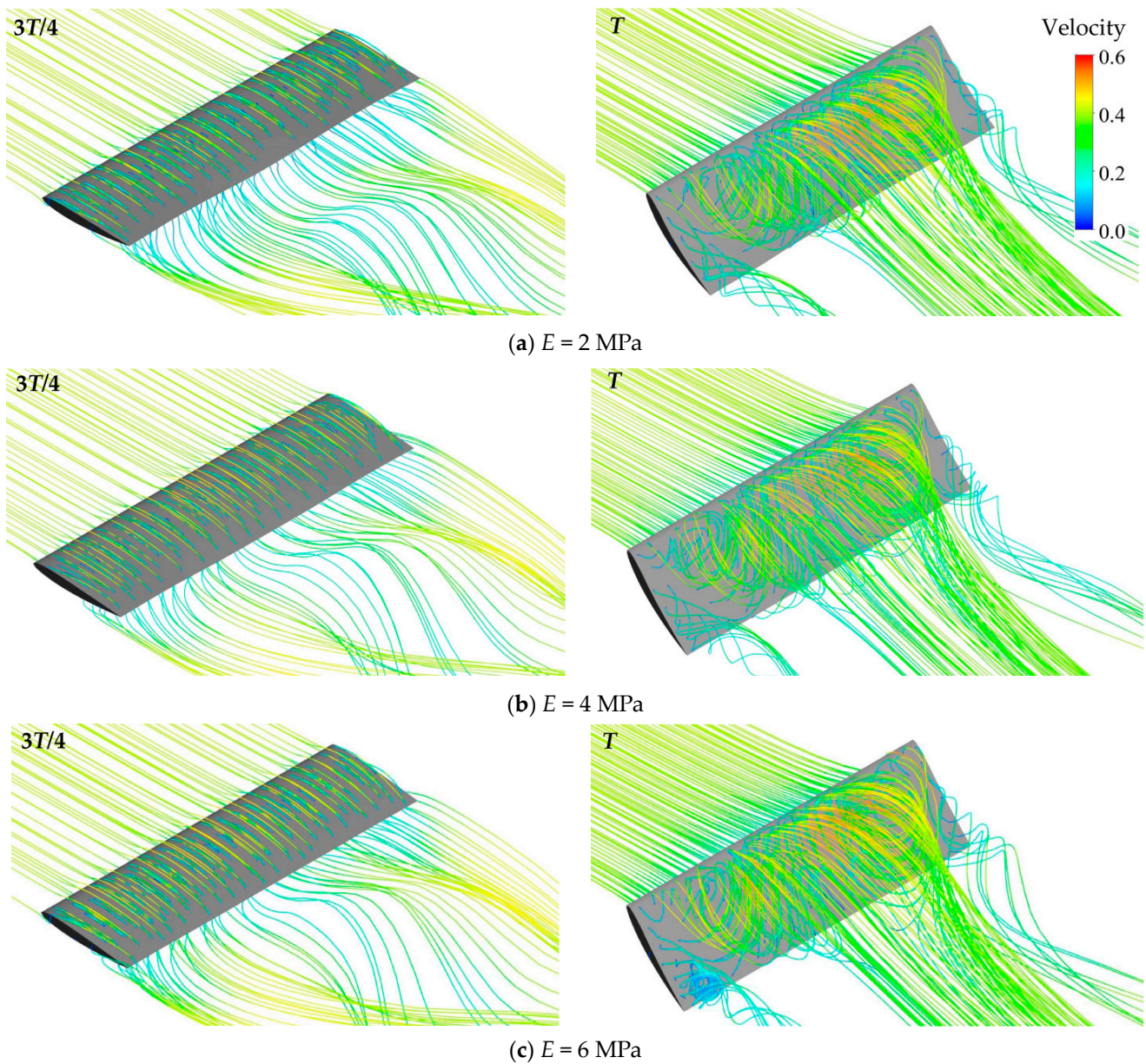


Figure 10. Three-dimensional streamlines around deformable hydrofoil.

The 2D streamlines and vortices around the rigid hydrofoil at various Z positions and elastic moduli are shown in Figures 11–13. The flow structures varied with Z position, elastic modulus, and deformation. For $E = 2$ MPa at $t = 3T/4$, as shown in Figure 11a, a counterclockwise LEV formed over the lower surface and developed downstream. A clockwise-attached vortex and TEV formed over the upper and trailing edges, respectively. The scale and intensity of TEV increased with increasing Z values.

At $t = T$, as shown in Figure 11b, a clockwise LEV formed and developed above the upper surface. The scale and intensity of TEV decreased with increasing Z values. At $Z = S/2$, the LEV remained attached to the upper surface. A slim-attached vortex formed between the upper surface and the LEV at $Z = 0-S/4$. The TEV formed, and its scale and intensity decreased with increasing Z values. At $Z = 0$ and $S/8$, the streamlines flipped over from the lower surface to the upper surface, bypassing the trailing edge caused by the TEV. This phenomenon disappears as the Z value increases.

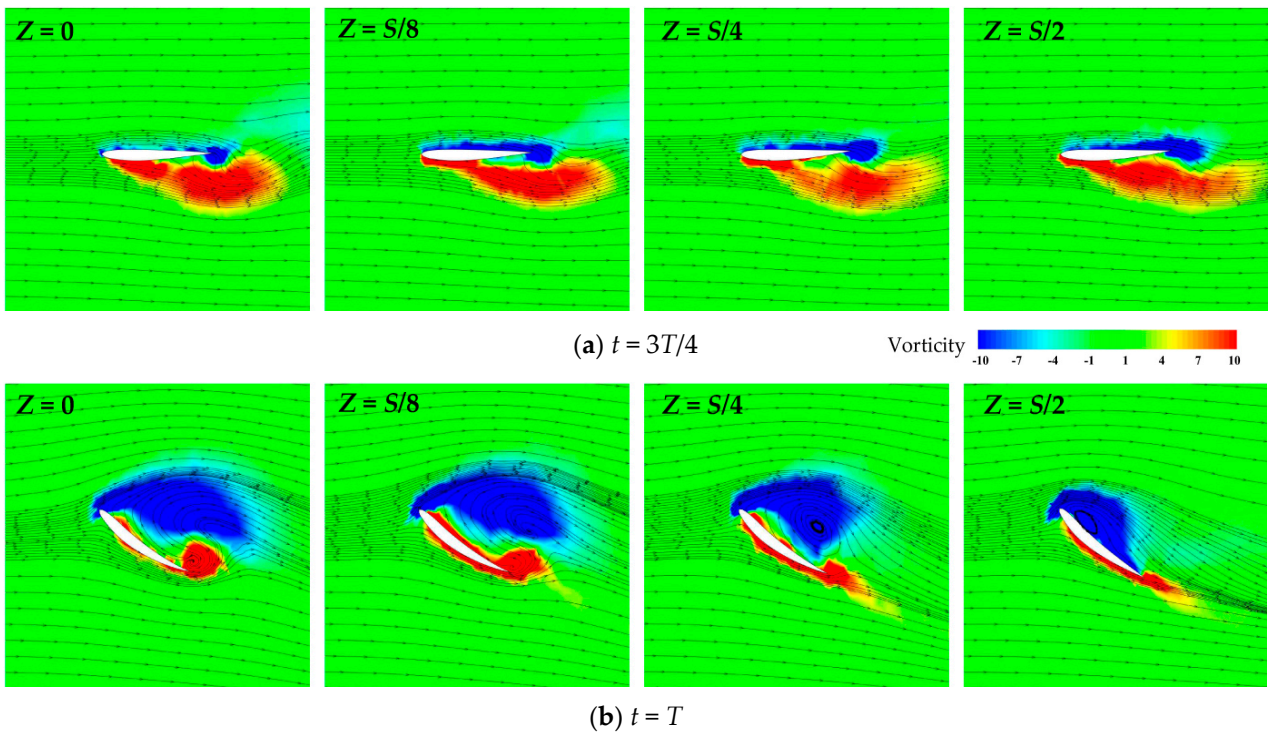


Figure 11. Flow structures at various Z positions for $E = 2$ MPa.

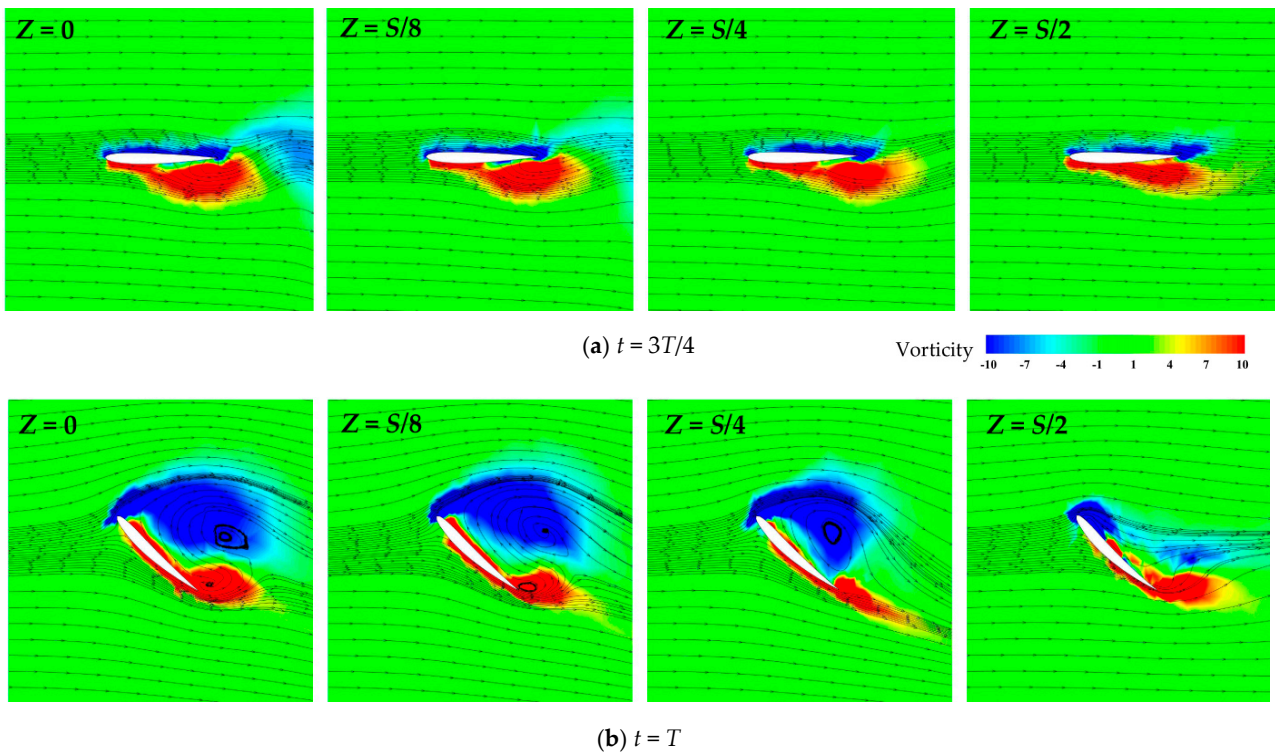


Figure 12. Flow structures at various Z positions for $E = 4$ MPa.

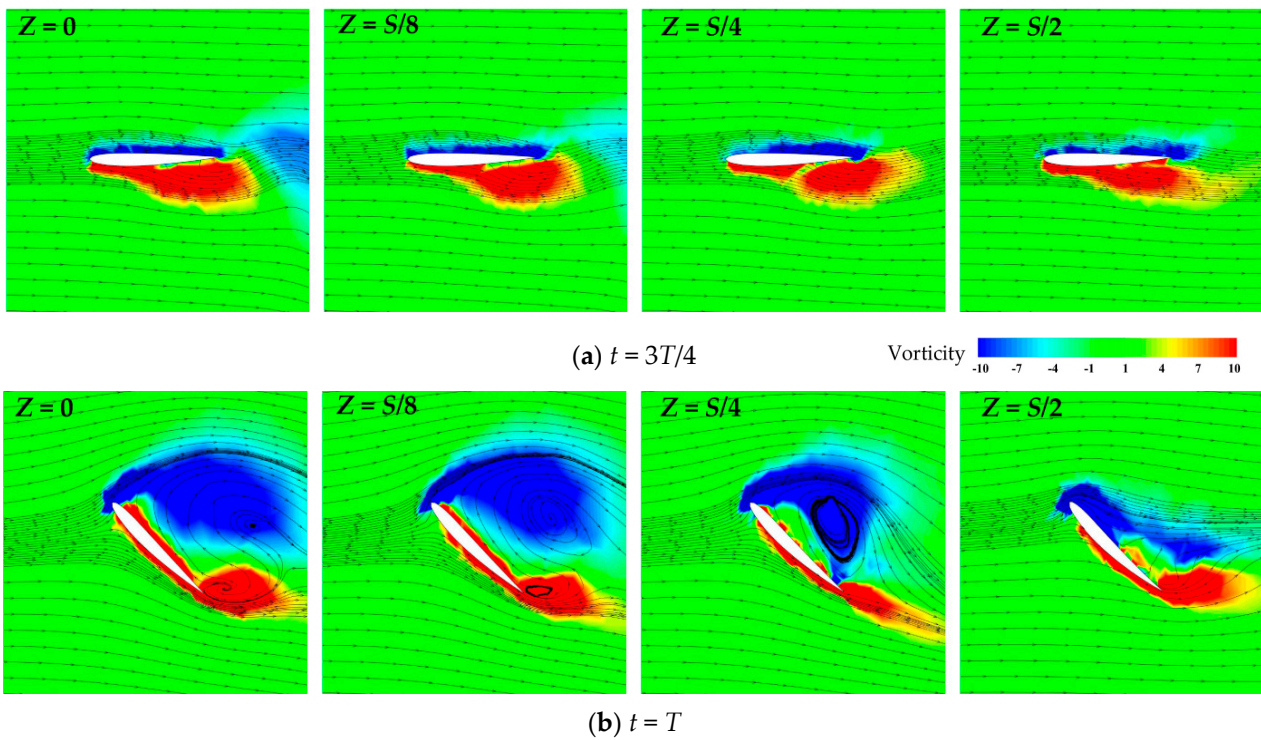


Figure 13. Flow structures at various Z positions for $E = 6$ MPa.

The flow patterns for $E = 4$ and 6 MPa were similar to those for $E = 2$ MPa. At $t = 3T/4$, as shown in Figures 8a, 11a, 12a and 13a, the scale and intensity of the LEV over the lower surface and TEV decreased with increasing elastic modulus. At $t = T$, as shown in Figures 8b, 11b, 12b and 13b, the scale and intensity of the TEV increased with increasing elastic modulus. Correspondingly, the streamlines near the trailing edge were more evidently deflected at a higher elastic modulus. The increased deformation encouraged the formation of the tip vortex, resulting in a more pronounced interference with the TEV. The above analysis implies that the deformations contribute to the suppression of the TEV and streamline deflection at large pitching angles. To clearly demonstrate the vertical structures, the flow structures at the typical time point T are shown in Figure 14.

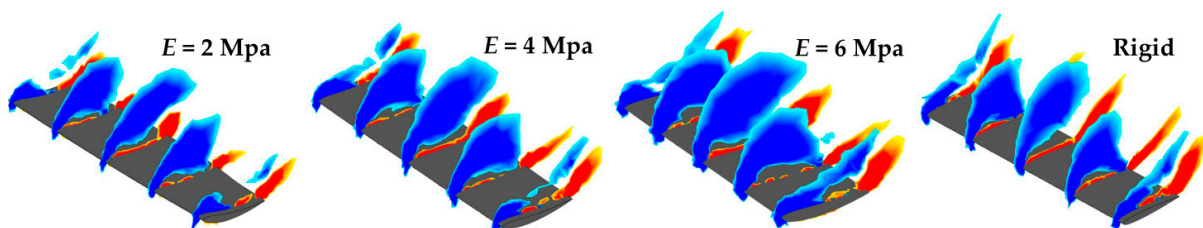


Figure 14. Flow structures at various elastic moduli ($t = T$).

The 3D deformation contours and pressure coefficients of the hydrofoil under various elasticity moduli at $t = 3T/4$ and T are shown in Figure 15. At a specific instant, the chordwise deformations at various cross-sections of Z/S varied due to distinct pressure distributions. Subsequently, these varying chordwise deformations caused spanwise deformation. Furthermore, the pressure distribution varied with the elastic modulus or deformation. The ensuing section delves into the interaction between deformation and pressure distribution.

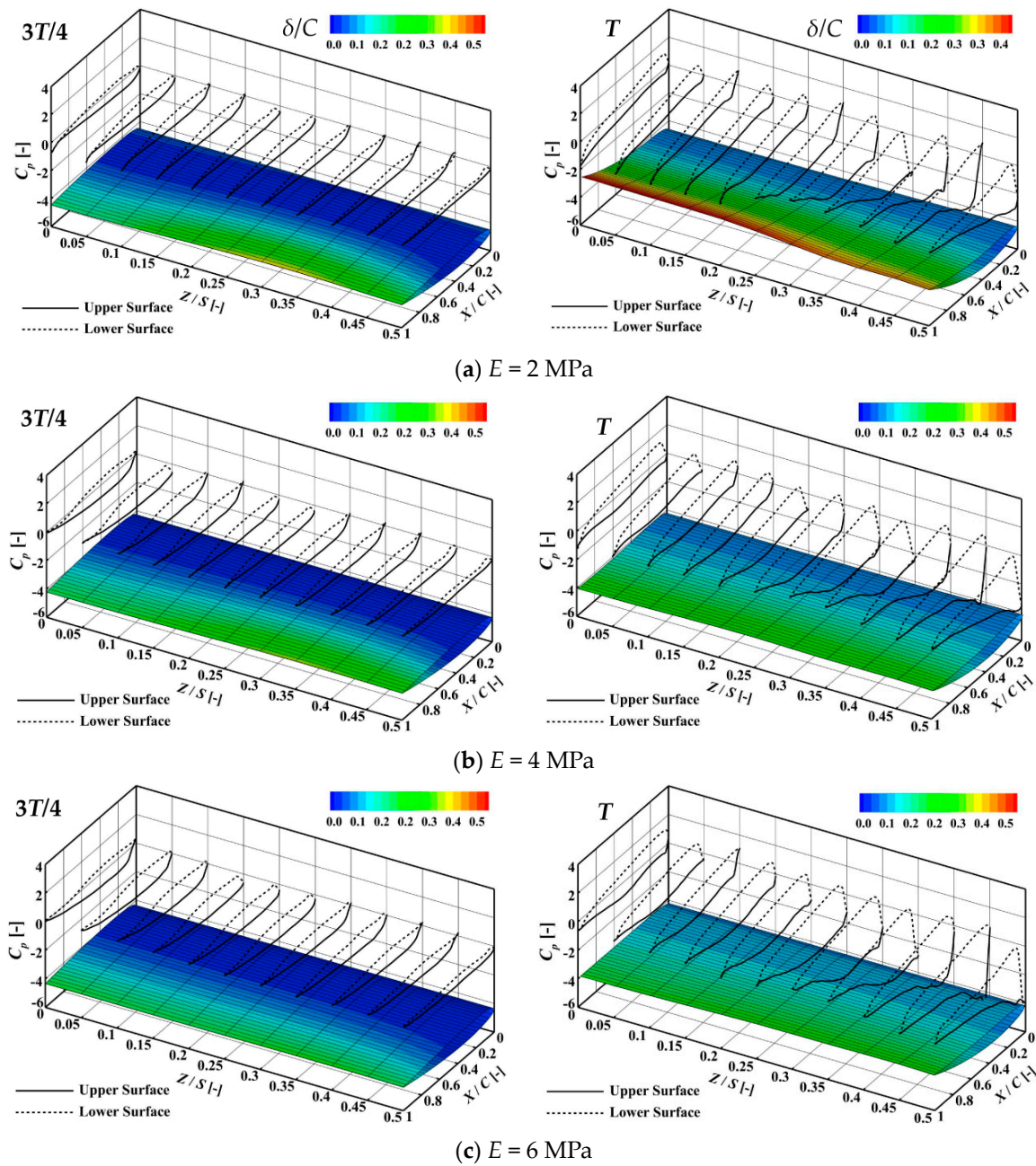


Figure 15. Deformation and pressure coefficient.

For $E = 2$ MPa, as shown in Figure 15a, the spanwise deformation modes at $t = 3T/4$ and T were different. The deformation first increased and then decreased as Z/S increased at $t = 3T/4$. However, the deformation decreased monotonically as Z/S increased at $t = T$. The pressure coefficient differences between the upper and lower surfaces were 1.04 and 0.92 at $Z/S = 0$ and 0.5, respectively. The maximum pressure coefficient difference of 1.52 was obtained at $Z/S = 0.2$. The lower pressure coefficient difference at $Z/S = 0.5$ caused decreased deformation. Owing to symmetry, the maximum deformation occurred at the midspan of the hydrofoil, even when the pressure coefficient difference was not at its maximum. The maximum non-dimensional deformations of the trailing edge at $t = 3T/4$ and T were 0.31 and 0.36, obtained at $Z/S = 0.3$ and 0, respectively. The overall deformation of the hydrofoil at $t = 3T/4$ was less than that at $t = T$. The difference in the pitching angle of the hydrofoil led to different flow structures and pressure distributions, which led to different deformations.

For $E = 4$ MPa, as shown in Figure 15b, the non-dimensional deformation first increased and then decreased as Z/S increased at $t = 3T/4$. The maximum deformation of the trailing edge at $t = 3T/4$ was 0.21, obtained at $Z/S = 0.35$. The pressure distribution around the hydrofoil at $t = T$ for $E = 4$ MPa was slightly different from that at $E = 2$ MPa. The maximum pressure coefficient difference was 1.90, obtained at $Z/S = 0.3$, which is closer to the tip. The elastic modulus was relatively large. As a result, the spanwise deformation tended to be more uniform than that for $E = 2$ MPa. Thus, the nondimensional deformation was slightly affected by the value of Z/S at $t = T$. The average value of the non-dimensional deformation of the trailing edge at various Z/S was 0.22.

For $E = 6$ MPa, as shown in Figure 15c, the pressure and deformation distributions were similar to those for $E = 4$ MPa. The effects of Z/S on the nondimensional deformation were limited at $t = 3T/4$ and T . The average values of the non-dimensional deformation of the trailing edge at various Z/S were 0.12 and 0.14 at $t = 3T/4$ and T , respectively.

The nondimensional deformation of the trailing edge based on chord length C is shown in Figure 16. The deformation magnitude decreased with an increase in the elasticity modulus. The pressure distributions around the hydrofoil at various elastic moduli exhibited significant discrepancies. It can be concluded that the deformation affects the pressure distribution.

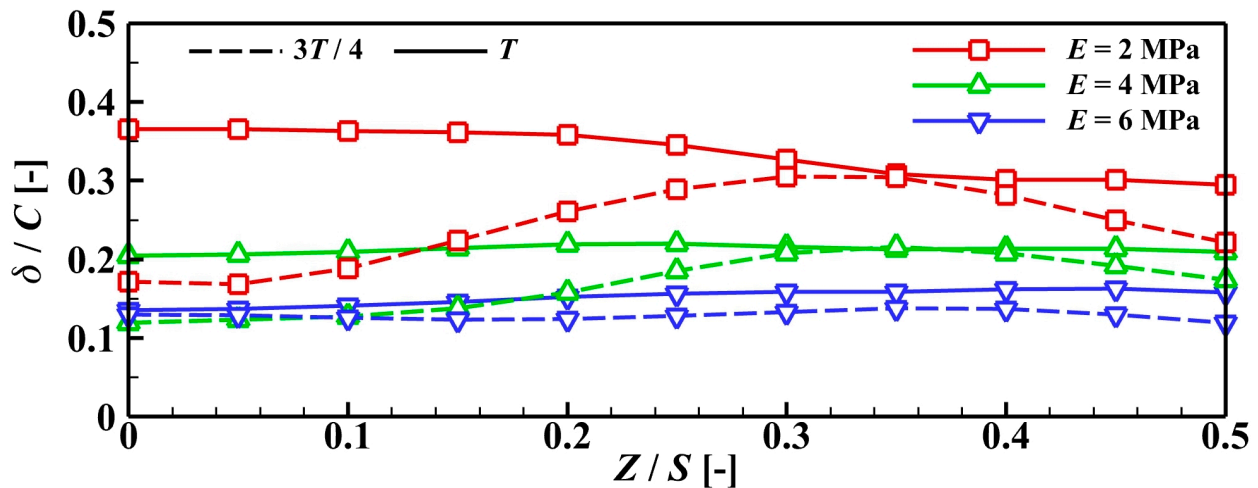


Figure 16. Spanwise deformation of trailing edge.

The averages and differences in the pressure coefficients over the upper and lower surfaces are shown in Figure 17. It is worth noting that for the rigid hydrofoil without deformation, the difference in the pressure coefficients decreases at $Z/S = 0.4-0.5$, which is near the hydrofoil tips. The decrease in the pressure coefficient difference was caused by the curling of the streamlines, as mentioned in Section 4.1. The magnitudes of the average and difference in the pressure coefficients increased with increasing elastic modulus. The pressure coefficients at $t = 3T/4$ were less affected by the elasticity modulus compared with those at $t = T$. Taking $t = T$ as an example, the large deformation for a low elasticity modulus indicated the obvious upward bending of the trailing edge. Subsequently, the angle of attack decreased correspondingly. Therefore, the positive pressure coefficient over the lower surface and the negative pressure coefficient over the upper surface both decreased, leading to a reduction in the difference in the pressure coefficient. Meanwhile, the drop in the pressure coefficient difference near the hydrofoil tips led to a reduction in the non-dimensional deformation, as shown in Figure 15.

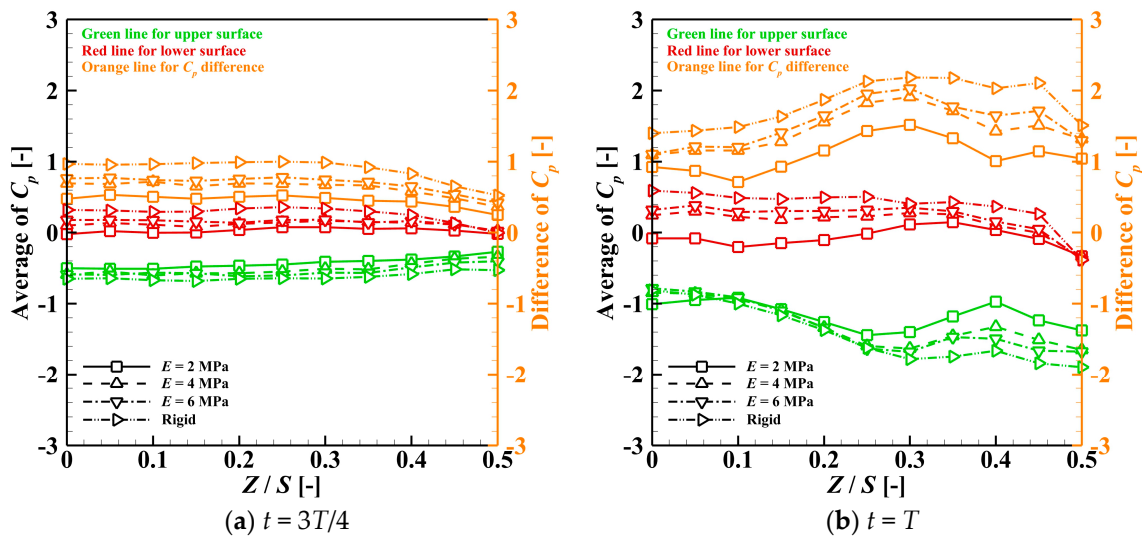


Figure 17. Average and difference of pressure coefficient for various elasticity moduli and Z positions.

4.3. Hydrodynamic Performance

The instantaneous coefficients of the lift, drag, and hydrodynamic torque are shown in Figure 18. The peak values of C_L , C_D , and C_M increased monotonically as the elasticity modulus increased and deformation decreased. This is consistent with the variation pattern of the pressure coefficient difference discussed in Section 4.2. This implies that the deformation of the hydrofoil plays an unfavorable role in improving the magnitude of hydrodynamic performance. It should be noted that the drag coefficient C_D is equal to or below 0 when $\alpha(t)$ ranges from 8° to 22° and from -22° to -8° . At this moment, the drag of the activated pitching hydrofoil converts to the thrust [19,20]. The drag–thrust transition is related to the value of the angle of attack, $\alpha_A(t) = \text{atan}(\alpha'(t)C/U) - \alpha(t)$. When the angle of attack is below 0, the hydrofoil generates the thrust, namely, the negative drag. According to the pitching motion and incident flow velocity, the calculated angle of attack is below 0. Therefore, the negative value of the drag coefficient is generated at certain moments.

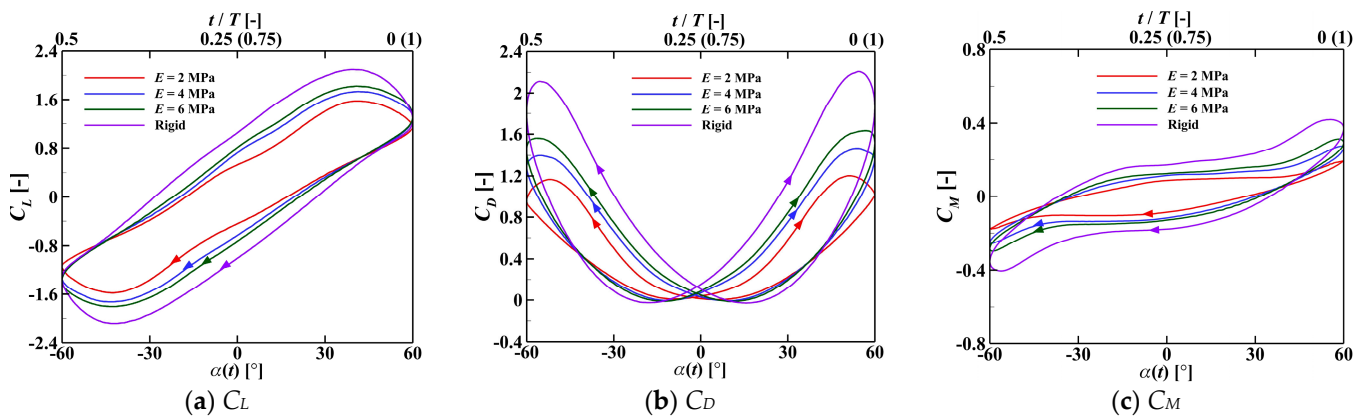


Figure 18. Hydrodynamic performance.

The hysteresis areas and intensities of the lift, drag, and torque coefficients at various elastic moduli are listed in Table 2. The hysteresis areas and intensities of C_L , C_D , and C_M increased monotonically as the elasticity modulus increased. These parameters serve as indicators of the amplitude of fluctuations in hydrodynamic forces. This implies that the degree of fluctuation of the lift, drag, and torque increases with an increase in the elasticity modulus. This fluctuation leads to the fatigue of the hydrofoil. The implementation of a deformable hydrofoil has the potential to mitigate load fluctuations, which is expected to extend the service life of the hydrofoil.

Table 2. The hysteresis area and intensity of C_L , C_D , and C_M .

	A_{CL}	A_{CD}	A_{CM}	K_{CL}	K_{CD}	K_{CM}
2 MPa	11.64	4.60	0.76	6.39	6.46	0.78
4 MPa	14.19	6.74	1.08	7.03	7.95	1.11
6 MPa	15.34	8.00	1.29	7.36	8.89	1.27
Rigid	18.34	12.68	2.11	8.47	12.06	1.69

5. Conclusions

This study examined the fluid–structure interaction of a deformable hydrofoil under the activated pitching mode using a 3D two-way FSI numerical model. The numerical model was established through the ANSYS Workbench 16.0 platform. We comprehensively analyzed flow structure, deformation in the chordwise and spanwise directions, pressure distribution, and hydrodynamic performance under various elastic moduli to unveil the fluid–structure interaction of the deformable hydrofoil.

An evident difference in flow structures, such as streamlines and vortices along the spanwise direction, was observed around the surface of the rigid hydrofoil. This difference led to a variation in pressure distribution along the spanwise direction, resulting in a decrease in pressure coefficients on the upper and lower surfaces near the tips of the hydrofoil. For a deformable hydrofoil, deformation occurs under hydrodynamic pressure, causing a difference in chordwise deformation along the spanwise direction, namely, the spanwise deformation. Furthermore, deformation has a significant impact on the flow structure and pressure distribution by altering the angle of attack of the hydrofoil. The difference in pressure coefficients between the upper and lower surfaces decreased with increasing deformation, significantly affecting the hydrodynamic performance. Within the tested parameters, the peak values of lift, drag, and torque coefficients decreased with increasing deformation. However, fluctuations in these coefficients decreased with increasing deformation, benefiting the service life of the hydrofoil. The results established a relationship between hydrodynamic performance and hydrofoil deformation, offering conclusive reference and technical support for TCE device blade design to achieve moderate deformation.

Based on the findings of this study, it is recommended that designers assess the hydrodynamic performance of hydrofoils subjected to various spanwise deformations, ensuring appropriate deformations for higher lift and lower fluctuation in lift, drag, and torque. Subsequently, careful selection of pitching amplitude and elastic modulus is crucial to control hydrofoil deformation.

In this study, we numerically investigated the hydrodynamic performance and interaction between the 3D deformation and 3D flow effects of a pitching hydrofoil. However, it is important to note that this study lacks pertinence to a specific TCE device, as energy-harvesting performance was not considered. In future research, we plan to establish numerical models for the HAT, VAT undergoing rotation, and oscillating hydrofoil undergoing heaving and pitching motions. We aim to explore the effects of 3D passive deformation on the energy-harvesting performance of various TCE devices.

Author Contributions: Conceptualization, methodology, software, validation, and investigation, H.Q.; data curation, methodology, software, supervision, X.D.; writing—original draft preparation, H.Q.; writing—review and editing, funding acquisition, X.L. All authors have read and agreed to the published version of the manuscript.

Funding: This research was funded by the Shandong Natural Science Foundation Youth Project (Grant Nos.: ZR2023QE075 and ZR2023QE110), the Open Project Program of Shandong Marine Aerospace Equipment Technological Innovation Center (Grant No.: MAETIC202210), the Yantai City Science and Technology Innovation Development Project (Grant No.: 2023XDRH016), and the Shandong Natural Science Foundation Project (Grant No.: ZR2022ME145).

Institutional Review Board Statement: Not applicable.

Informed Consent Statement: Not applicable.

Data Availability Statement: Data are unavailable due to privacy restrictions.

Conflicts of Interest: The authors declare no conflicts of interest.

References

1. Liu, Z.; Qu, H.; Shi, H. Numerical study on hydrodynamic performance of a fully passive flow driven pitching hydrofoil. *Ocean Eng.* **2019**, *177*, 70–84. [[CrossRef](#)]
2. Huera-Huarte, F. Pitching foil propulsion performance decays near the free surface. *Ocean Eng.* **2023**, *272*, 113663. [[CrossRef](#)]
3. Mamouri, A.; Khoshnevis, A.; Lakzian, E. Experimental study of the effective parameters on the offshore wind turbine's airfoil in pitching case. *Ocean Eng.* **2020**, *198*, 106955. [[CrossRef](#)]
4. Zhu, C.; Qiu, Y.; Wang, T. Dynamic stall of the wind turbine airfoil and blade undergoing pitch oscillations: A comparative study. *Energy* **2021**, *222*, 120004. [[CrossRef](#)]
5. Zhang, M.; Wang, M.; Kang, Z.; Liu, T. Hydrodynamic characteristics of a pitching hydrofoil in unsteady uniform inflow with special emphasis on the hysteresis effect. *Ocean Eng.* **2023**, *269*, 113596. [[CrossRef](#)]
6. Zhang, M.; Wu, Q.; Wang, G.; Huang, B.; Fu, X.; Chen, J. The flow regime and hydrodynamic performance for a pitching hydrofoil. *Renew. Energy* **2020**, *150*, 412–427. [[CrossRef](#)]
7. Alam, M.; Muhammad, Z. Dynamics of flow around a pitching hydrofoil. *J. Fluids Struct.* **2020**, *99*, 103151. [[CrossRef](#)]
8. Nachtane, M.; Tarfaoui, M.; Goda, I.; Rouway, M. A review on the technologies, design considerations and numerical models of tidal current turbines. *Renew. Energy* **2020**, *157*, 1274–1288. [[CrossRef](#)]
9. Rad, M.; Khoshnevis, A. Experimental investigation of flow structure over pitching airfoil in the wake of circular cylinder. *Ocean Eng.* **2023**, *284*, 115103.
10. Dai, Y.; Xia, Y.; Huang, G.; Yang, C.; Li, Y. Performance improvement of a wing with a controlled spanwise bending wingtip. *Ocean Eng.* **2023**, *287*, 115795. [[CrossRef](#)]
11. Xiao, Q.; Zhu, Q. A review on flow energy harvesters based on flapping foils. *J. Fluids Struct.* **2014**, *46*, 174–191. [[CrossRef](#)]
12. Wu, X.; Zhang, X.; Tian, X.; Li, X.; Lu, W. A review on fluid dynamics of flapping foils. *Ocean Eng.* **2023**, *195*, 106712. [[CrossRef](#)]
13. Rostami, A.; Armandei, M. Renewable energy harvesting by vortex-induced motions: Review and benchmarking of technologies. *Renew. Sustain. Energy Rev.* **2017**, *70*, 193–214. [[CrossRef](#)]
14. Tong, H.; Wang, Y. Experimental study on unsteady aerodynamic characteristics of deformed blades for vertical axis wind turbines. *Renew. Energy* **2021**, *173*, 808–826. [[CrossRef](#)]
15. Lee, H.; Kwon, O. Performance improvement of horizontal axis wind turbines by aerodynamic shape optimization including aeroelastic deformation. *Renew. Energy* **2020**, *147*, 2128–2140. [[CrossRef](#)]
16. Li, Y.; Pan, Z.; Zhang, N. Propulsive properties of a flexible oscillating wing with time-varying camber deformation. *Ocean Eng.* **2021**, *235*, 109332. [[CrossRef](#)]
17. Guo, H.; Hu, J.; Guo, C.; Zhang, W.; Lin, J. Numerical simulation of the dynamic stall of a freely rotating hydrofoil. *Phys. Fluids* **2020**, *32*, 095113. [[CrossRef](#)]
18. Seshadri, P.; Aravind, A.; De, A. Leading edge vortex dynamics in airfoils: Effect of pitching motion at large amplitudes. *J. Fluids Struct.* **2023**, *116*, 103796. [[CrossRef](#)]
19. Chao, L.; Pan, G.; Zhang, D.; Yan, G. Numerical investigations on the force generation and wake structures of a nonsinusoidal pitching foil. *J. Fluids Struct.* **2019**, *85*, 27–39. [[CrossRef](#)]
20. Chao, L.; Pan, G.; Zhang, D.; Yan, G. On the drag–thrust transition of a pitching foil. *Ocean Eng.* **2019**, *192*, 106564. [[CrossRef](#)]
21. Yin, T.; Pavesi, G. Dynamic responses of pitching hydrofoil in laminar–turbulent transition regime. *J. Fluids Struct.* **2022**, *111*, 103544. [[CrossRef](#)]
22. Zhu, C.; Feng, Y.; Shen, X.; Dang, Z.; Chen, J.; Qiu, Y.; Wang, T. Effects of the height and chordwise installation of the vane-type vortex generators on the unsteady aerodynamics of a wind turbine airfoil undergoing dynamic stall. *Energy* **2023**, *266*, 126418. [[CrossRef](#)]
23. Liu, Z.; Qu, H. Numerical study on a coupled-pitching flexible hydrofoil under the semi-passive mode. *Renew. Energy* **2022**, *189*, 339–358. [[CrossRef](#)]
24. Wang, Y.; Tong, H.; Sima, H.; Wang, J.; Sun, J.; Huang, D. Experimental study on aerodynamic performance of deformable blade for vertical axis wind turbine. *Energy* **2019**, *181*, 187–201. [[CrossRef](#)]
25. Qian, Y.; Zhang, Y.; Sun, Y.; Wang, T. Numerical investigations of the flow control effect on a thick wind turbine airfoil using deformable trailing edge flaps. *Energy* **2023**, *265*, 126327. [[CrossRef](#)]
26. Zhang, Y.; Wang, Y.; Xie, Y.; Sun, G.; Han, J. Effects of flexibility on energy extraction performance of an oscillating hydrofoil under a semi-activated mode. *Energy* **2022**, *242*, 122940. [[CrossRef](#)]
27. Zhang, Y.; Wang, Y.; Han, J.; Sun, G.; Xie, Y. Effects of hydrofoil motion parameters and swing arm parameters on power extraction of a flexible hydrofoil in swing arm mode. *Ocean Eng.* **2022**, *245*, 110543. [[CrossRef](#)]
28. Zhang, Y.; Wang, Q.; Han, J.; Xie, Y. Effects of unsteady stream on hydrodynamic behavior of flexible hydrofoil in semi-passive mode. *Renew. Energy* **2023**, *206*, 451–465. [[CrossRef](#)]
29. Jeanmonod, G.; Oliver, M. Effects of chordwise flexibility on 2D flapping foils used as an energy extraction device. *J. Fluids Struct.* **2017**, *70*, 327–345. [[CrossRef](#)]

30. Siala, F.; Fard, K.; Liburdy, J. Experimental study of inertia-based passive flexibility of a heaving and pitching airfoil operating in the energy-harvesting regime. *Phys. Fluids* **2020**, *32*, 017101. [[CrossRef](#)]
31. Kinsey, T.; Dumas, G. Three-dimensional effects on an oscillating-foil hydrokinetic turbine. *J. Fluids Eng.* **2012**, *134*, 071105. [[CrossRef](#)]
32. Hu, J.; Xiao, Q. Three-dimensional effects on the translational locomotion of a passive heaving wing. *J. Fluids Struct.* **2014**, *46*, 77–88. [[CrossRef](#)]
33. Deng, J.; Caulfield, C.P.; Shao, X. Effect of aspect ratio on the energy extraction efficiency of three-dimensional flapping foils. *Phys. Fluids* **2014**, *26*, 043102. [[CrossRef](#)]
34. Kim, D.; Strom, B.; Mandre, S.; Breuer, K. Energy-harvesting performance and flow structure of an oscillating hydrofoil with finite span. *J. Fluids Struct.* **2017**, *70*, 314–326. [[CrossRef](#)]
35. Oksuz, S.; Celik, F.; Bayraktar, S. Three-dimensional computational analysis of flow over twisted hydrofoils. *Ocean Eng.* **2023**, *267*, 113304. [[CrossRef](#)]
36. Herath, M.; Phillips, A.; John, N.; Brandner, P.; Pearce, B.; Prusty, G. Hydrodynamic response of a passive shape-adaptive composite hydrofoil. *Mar. Struct.* **2021**, *80*, 103084. [[CrossRef](#)]
37. Huang, Z.; Xiong, Y.; Xu, Y. The simulation of deformation and vibration characteristics of a flexible hydrofoil based on static and transient FSI. *Ocean Eng.* **2019**, *182*, 61–74. [[CrossRef](#)]
38. Mamouri, A.; Lakzian, E.; Khoshnevis, A. Entropy analysis of pitching airfoil for offshore wind turbines in the dynamic stall condition. *Ocean Eng.* **2019**, *187*, 106229. [[CrossRef](#)]
39. Mamouri, A.; Khoshnevis, A.; Lakzian, E. Entropy generation analysis of S825, S822, and SD7062 offshore wind turbine airfoil geometries. *Ocean Eng.* **2019**, *173*, 700–715. [[CrossRef](#)]
40. Zhu, C.; Wu, J.; Wang, T. Dynamic stall control of the wind turbine airfoil via single-row and double-row passive vortex generators. *Energy* **2019**, *189*, 116272. [[CrossRef](#)]
41. Lee, J.S.; Lee, S.H. Fluid–structure interaction analysis on a flexible plate normal to a free stream at low Reynolds numbers. *J. Fluids Struct.* **2012**, *29*, 18–34. [[CrossRef](#)]
42. Gluck, M.; Breuer, M.; Durst, F.; Halfmann, A.; Rank, E. Computation of fluid–structure interaction on light weight structures. *J. Wind Eng. Ind. Aerodyn.* **2001**, *89*, 1351–1368. [[CrossRef](#)]
43. Liu, Z.; Qu, H.; Song, X. Experimental and numerical studies on a passively deformed coupled-pitching hydrofoil under the semi-activated mode. *Renew. Energy* **2024**, *227*, 120559. [[CrossRef](#)]
44. Kim, D.; Chang, J. Low-Reynolds-number effect on the aerodynamic characteristics of a pitching NACA0012 airfoil. *Aerosp. Sci. Technol.* **2014**, *32*, 162–168. [[CrossRef](#)]

Disclaimer/Publisher’s Note: The statements, opinions and data contained in all publications are solely those of the individual author(s) and contributor(s) and not of MDPI and/or the editor(s). MDPI and/or the editor(s) disclaim responsibility for any injury to people or property resulting from any ideas, methods, instructions or products referred to in the content.